Supplementary information

Descriptor-based graded electrode microstructures design strategies of lithium-ion batteries for enhanced rate performance

Qiang Shan, Yuwen Liu, Shengli Chen*

Hubei Key Laboratory of Electrochemical Power Sources, Department of Chemistry,

Wuhan University, Wuhan 430072, China

S1. 3D microstructure-based (no volume-averaging) model of LIBs

S1.1 Governing equations

Supplementary table. 1. Model equations for each domain in the 3D microstructure-based electrochemical model [4].

Domain	Equations	Number
Pore domain (Electrolyte)	The generalized Nernst–Planck equation: $\frac{\partial c_{Li^+(l)}}{\partial t} = -\nabla\left(-\tilde{D}_{amb,Pore,eff}\nabla c_{Li^+(l)}\right) - \nabla\cdot\left(\frac{t_+ i_l}{F}\right)$	(1)
	$\tilde{D}_{amb} = t_+\tilde{D}_- + (1-t_+)\tilde{D}_+ \quad \tilde{D}_{amb,Pore,eff} = \tilde{D}_{amb}\cdot\frac{\varepsilon_{Pore}}{\tau^2_{Pore}}\cdot\frac{\varepsilon_{Electrolyte\ in\ Pore}}{\tau^2_{Electrolyte\ in\ Pore}}$	
	The charge conservation equation (electroneutrality equation): $i_l = -\kappa_{Pore,l,eff}\nabla\phi_l + \frac{2RT\kappa_{Pore,l,eff}}{c_{Li^+(l)}F^2}\left(1+\frac{\partial \ln f_\pm}{\partial \ln c_{Li^+(l)}}\right)(1-t_+)F\nabla c_{Li^+(l)}$	(2)
	$\kappa_l = \kappa_+ + \kappa_- \quad \kappa_{Pore,l,eff} = \kappa_l\cdot\frac{\varepsilon_{Pore}}{\tau^2_{Pore}}\cdot\frac{\varepsilon_{Electrolyte\ in\ Pore}}{\tau^2_{Electrolyte\ in\ Pore}}$	
Pore domain (CBD)	The charge conservation equation (Ohm's law): $i_e = -\sigma_{Pore,e,eff}\nabla\phi_e$	(3)
	$\sigma_{PCB,e,eff} = \sigma_e\cdot\frac{\varepsilon_{Pore}}{\tau^2_{Pore}}$	
NMC particles	The mass conservation equation (Fick's law): $\frac{\partial c_{Li^+(s)}}{\partial t} = -\nabla\left(-D_{c_{Li^+(s)}}\nabla c_{c_{Li^+(s)}}\right)$	(4)
Separator	The generalized Poisson–Nernst–Planck equation: $\frac{\partial c_{Li^+(l)}}{\partial t} = -\nabla\left(-\tilde{D}_{amb,Sep,eff}\nabla c_{Li^+(l)}\right) - \nabla\cdot\left(\frac{t_+ i_l}{F}\right)$	(5)
	The charge conservation equation (electroneutrality equation): $i_l = -\sigma_{Sep,l,eff}\nabla\phi_l + \frac{2RT\sigma_{Sep,l,eff}}{c_{Li^+(l)}F^2}\left(1+\frac{\partial \ln f_\pm}{\partial \ln c_{Li^+(l)}}\right)(1-t_+)F\nabla c_{Li^+(l)}$	
	The Bruggemann equation: $\tilde{D}_{amb,Sep,eff} = \tilde{D}_{amb}\cdot\varepsilon_{Pore\ in\ Sep}{}^{-0.5} \quad \sigma_{Sep,l,eff} = \sigma_l\cdot\varepsilon_{Pore\ in\ Sep}{}^{-0.5}$	
Electrolyte /NMC interface	The Butler-Volmer equation: $i_{ct} = i_0\left[\exp\left(\frac{\alpha_a F}{RT}\eta\right) - \exp\left(-\frac{\alpha_c F}{RT}\eta\right)\right] \quad \eta = \phi_e - \phi_l - OCV$	(6)

	The local exchange current density: $i_0 = nFKc_l^{*\frac{\alpha_a}{n}}\left(c_{s,max}^* - c_s^*\right)^{\frac{\alpha_a}{n}} c_s^{*\frac{\alpha_c}{n}}$	

S1.2 Initial and boundary conditions

An initial active material concentration, $c_{s,0}$, is prescribed, while the electrolyte initial concentration is given by $c_{l,0}$. An initial active material potential, OCV, is prescribed, while the electrolyte initial potential is given by 0. The boundary conditions are given in the following table.

Supplementary table. 2. Boundary conditions for each interface in the 3D microstructure-based electrochemical model [4].

Interface	Equations	Number
Electrode /Current collector	$n \cdot i_l = 0$	(7)
	$n \cdot i_e = i_{app}$	
	$i_{app} = \left(c_{s,max} - c_{s,0}\right) V_{AM} \frac{F}{3600} \frac{C_{rate}}{A_e}$	
Electrolyte /NMC	$n \cdot i_e = i_{ct}$	(8)
	$n \cdot i_l = i_{ct}$	
Li metal	$\phi_e = 0$	(9)

S1.3 Material parameters

The ambipolar diffusion coefficient of the binary electrolyte was defined as a function of the electrolyte concentration ($c_{Li^+(l)}$) and temperature (T) as:

$$\widetilde{D}_i = 10^{-4} \times 10^{-4.43 - \left(\frac{54}{\left(T - 229 - 5.0\times10^{-3} c_{Li^+(l)}\right)}\right) - 0.22\times10^{-3} c_{Li^+(l)}} \quad (10)$$

The ionic conductivity for the binary electrolyte was defined as a function of the electrolyte concentration ($c_{Li^+(l)}$) and temperature (T) as:

$$\kappa_i = 10^{-4} \times c_i(-10.5 + 0.668 \times 10^{-3}c_i + 0.494 \times 10^{-6}{c_i}^2 + 0.074T$$
$$- 1.78 \times 10^{-5}c_iT - 8.86 \times 10^{-10}{c_i}^2T \quad (11)$$
$$- 6.96 \times 10^{-5}T^2 + 2.80 \times 10^{-8}c_iT^2)^2$$

The transference number was defined as a function of the electrolyte concentration ($c_{Li^+(l)}$) as:

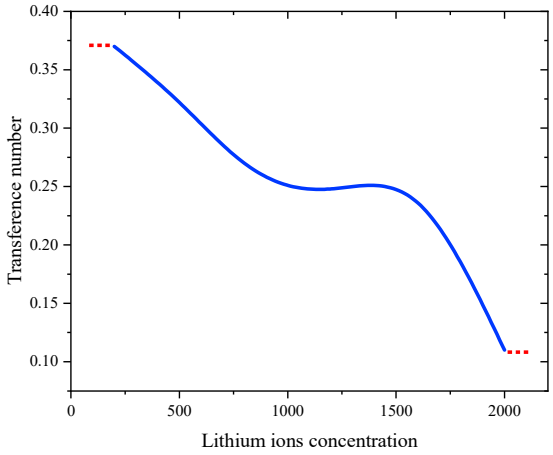

Supplementary Fig. 1. The concentration dependence of transference number.

The thermodynamic factor was defined as a function of the electrolyte concentration ($c_{Li^+(l)}$) as:

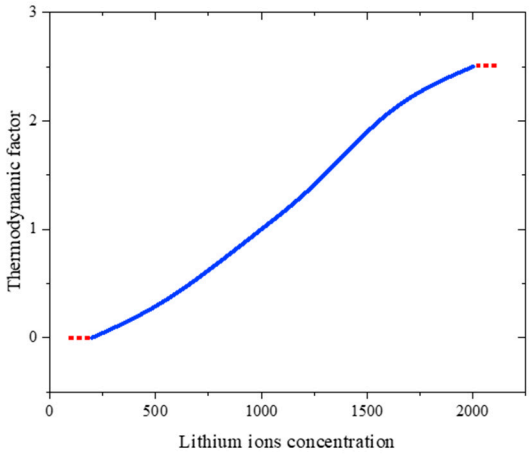

Supplementary Fig. 2. The concentration dependence of thermodynamic factor.

S1.3 Material parameters

Supplementary table. 3. Material properties and model parameters.

Parameter	Unit	Value	Source
t_{Li+}	1	Fig. 1	Nyman et al. [1]
$\frac{\partial \ln f_{\pm}}{\partial \ln c_{Li^+(l)}}$	1	Fig. 2	Zavalis et al. [2]
$\widetilde{D}_i$	$m^2\ s^{-1}$	Eq. (10)	Cai et al. [3]
κ_i	$S\ m^{-1}$	Eq. (11)	Cai et al. [3]
$c_{l,0}$	$mol\ m^{-3}$	1000	--
D_s	$m^2\ s^{-1}$	2×10^{-14}	Lu et al. [4]
$c_{s,max}$	$mol\ m^{-3}$	49000	Zheng et al. [5]
σ_{e^-}	$S\ m^{-1}$	1.039×10^{-3}	Park et al. [6]
$c_{s,0}$	$mol\ m^{-3}$	2810	--
V_{AM}	m^3	1.199×10^{-13}	--
σ_{l^-}	$S\ m^{-1}$	375	Liu et al. [7]
α_a	1	0.5	--
α_c	1	0.5	--
K_a	$m^{5/2}\ s^{-1}\ mol^{-1/2}$	2.07×10^{-10}	Danner et al. [8]
K_c	$m^{5/2}\ s^{-1}\ mol^{-1/2}$	5.24×10^{-11}	Danner et al. [8]
OCV	V	Fig. 3	Ebner et al. [9]
R	$J\ mol^{-1}\ K^{-1}$	8.314	--
T	K	298	--

Note: the mass density of NMC111 used in the study is $4.7\ g\ cm^{-3}$ [4], and the loading is $5.64 * 10^{-7}$ g.

S1.4 Nomenclature

Supplementary table. 4. Nomenclature

Nomenclature			
c	Concentration $(\mathrm{mol\ m^{-3}})$	**Superscript**	
D	Diffusion coefficient $(\mathrm{m^2\ s^{-1}})$	$\sim$	Chemical diffusion
t	Time (s)	$*$	Surface
i	Current density $(\mathrm{A\ m^{-2}})$		
t	Transfer number	**Subscript**	
ε	Porosity	s	Solid
τ	Tortuosity	0	Initial
κ	Ion conductivity $(\mathrm{S\ cm^{-1}})$	a	Anode
ϕ	Electrical potential (V)	c	Cathode
F	Farady constant $(96485\ \mathrm{C\ mol^{-1}})$	l	Electrolyte
R	Gas constant $(8.314\ \mathrm{J\ mol^{-1}\ K^{-1}})$	max	Maximum
T	Temperature (K)	$+$	Positive ion
$f_{\pm}$	Activity	eff	Efficient
σ	Electron conductivity $(\mathrm{S\ cm^{-1}})$	app	Applied
α	Transfer coefficient	sep	Separator
η	Overpotential (V)	e	Electron
K	Reaction rate constant	Pore	Pore domain
n	Charge number	AM	Active material
V	Volume $(\mathrm{m^3})$	ct	Charge transfer
OCV	Equilibrium potential (V)	$-$	Nagative ion
A_e	Electrode cross-sectional area $(\mathrm{m^2})$	amb	Ambipolar
C_{rate}	Rate of discharge/charge		

S1.5 Abbreviation

Supplementary table. 5. Abbreviation

Abbreviation			
LIBs	Lithium-ion batteries	DoD	Depth of discharge
SoL	State of lithium	dSoL	Time differential of SoL
SST	Solid-state transport	ΔSoL	Span of SoL
LST	Liquid-state transport	CC	Constant currents
EVs	Electric vehicles	NMC111	$LiNi_{1/3}Mn_{1/3}Co_{1/3}O_2$
P2D	Pseudo-two-dimension	CBD	Carbon binder domain
OCV	Open circuit potential	PARDISO	Parallel dDirect sSparse

S2. Comparation of the experimental and simulated discharge voltage response

The voltage response at C/20 is used as the open-circuit potential (OCV) of NMC111 vs. Li/Li^+.

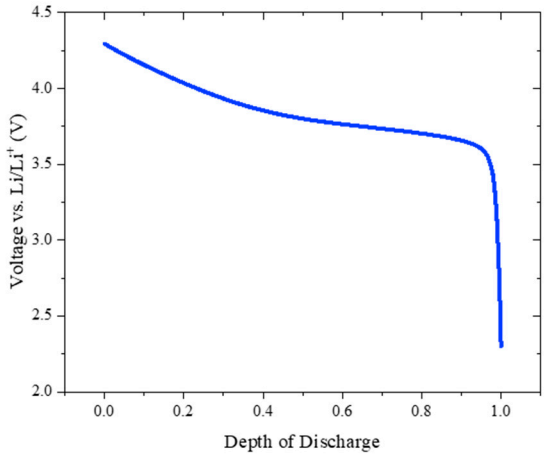

Supplementary Fig. 3. The OCV vs. DoD used for the modelling.

The particle size distribution data of NMC111 and electrochemical test datasets used in the study are derived from the ETH Zurich library, which is available open source from download at http://dx.doi.org/10.5905/ethz-iis-1.

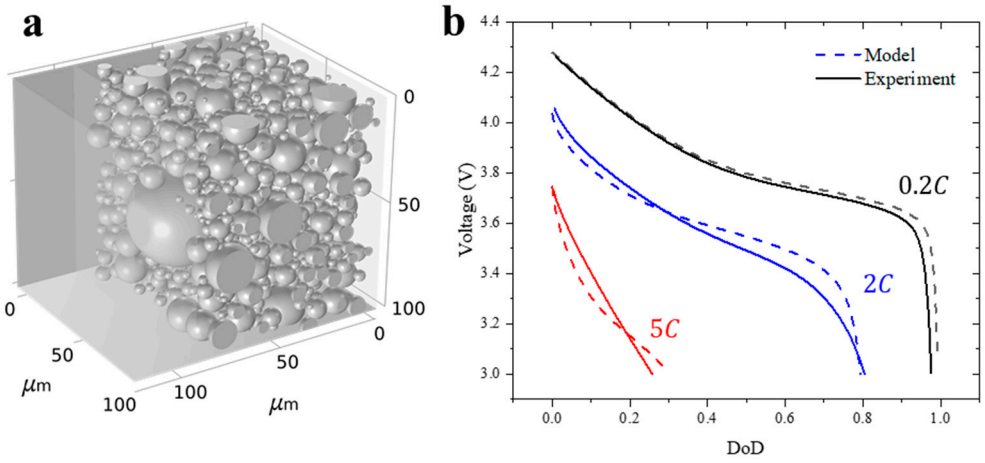

Supplementary Fig. 4. The comparison of the experimental and simulated discharge response: (a) reconstructed NMC111 electrode structure; (b) comparison of the

experimental and simulated discharge voltage response for a 92 μm electrode with 46% macro-porosity at discharge rates of 0.2C, 2C, and 5C.

S3. Selection of graded porosity design scheme

Here, six types of graded porosity scheme are used. The porosity increases/reduces by shrinking/expanding CBD, while the NMC particles are unchanged. The volume ratio of the constituents for the electrolyte and CBD and corresponding porosity (in blue) in the four regions as shown in the following table.

Supplementary table 6. Graded porosity design schemes

Region	I	II	III	IV
Basic	0.312 (60:40)	0.312 (60:40)	0.312 (60:40)	0.312 (60:40)
Scheme1	0.416 (80:20)	0.364 (70:30)	0.260 (50:50)	0.208 (40:60)
Scheme2	0.416 (80:20)	0.364 (70:30)	0.312 (60:40)	0.156 (30:70)
Scheme3	0.416 (80:20)	0.416 (80:20)	0.260 (50:50)	0.156 (30:70)
Scheme4	0.468 (90:10)	0.364 (70:30)	0.312 (60:40)	0.156 (30:70)
Scheme5	0.468 (90:10)	0.416 (80:20)	0.208 (40:60)	0.156 (30:70)
Scheme6	0.468 (90:10)	0.468 (90:10)	0.156 (30:70)	0.156 (30:70)

Results indicate that the capacity performance of the electrode with scheme6 increases by up to 39% at 5C. Therefore, scheme6 is chosen as the scheme for graded porosity design.

S4. Details of determining the SST-dominant depth and the penetration depth

The time differential of the average state of lithium (dSoL) of model 1, model 2, and model 3 are shown here. As seen in **Supplementary Fig. 5,** according to the rules

of determining the SST-dominant depth and the penetration depth in the text, the SST-dominant depth of model 1, model 2, and model 3 are 25 μm, 43 μm, and 40 μm, respectively; and the penetration depth of model 1, model 2, and model 3 are 76 μm, 100 μm, and 100 μm, respectively.

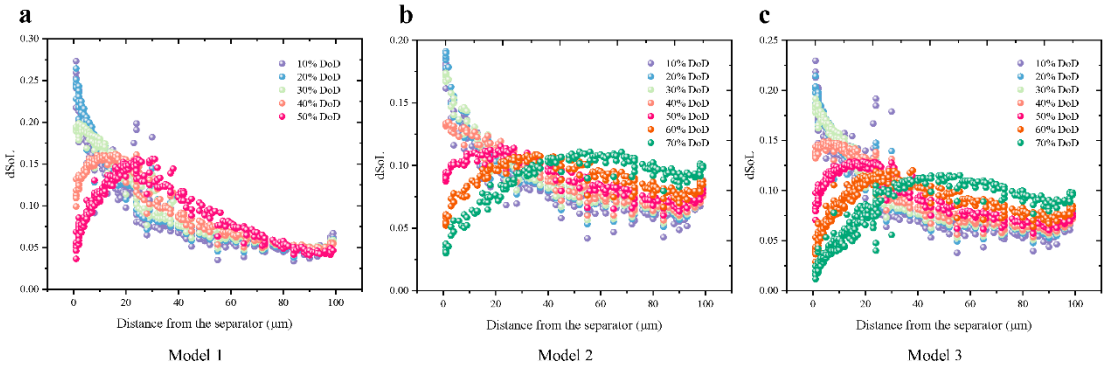

Supplementary Fig. 5. The time differential of the average state of lithium (dSoL) for different models: (a) model 1; (b) model 2; (c) model 3.

S5. The 3D SoL distribution of particles for different models at the end stage of discharge

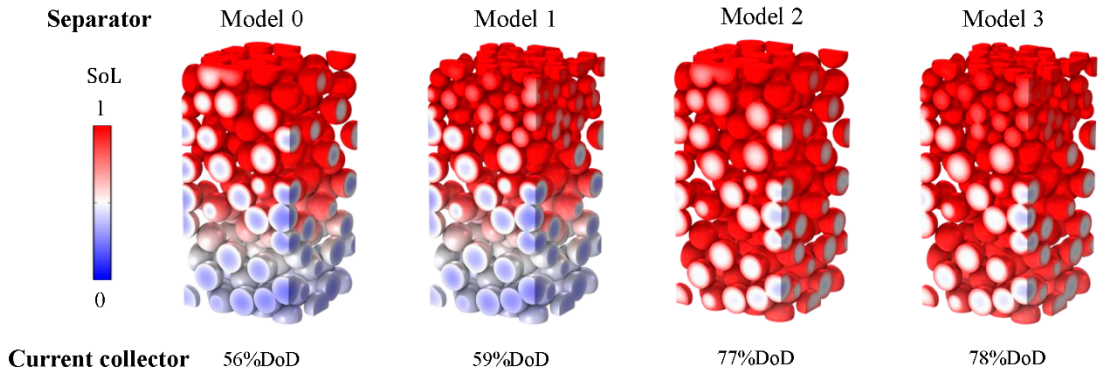

Supplementary Fig. 6. The 3D SoL distribution of particles for model 0 at 56% DoD, model 1 at 59% DoD, model 2 at 77% DoD, model 3 at 78% DoD, respectively.

Supplementary references

[1] A. Nyman, M. Behm, and G. Lindbergh, “Electrochemical characterisation and modelling of the mass transport phenomena in $LiPF_6$-EC-EMC,” Electrochim. Acta, vol. 53, p. 6356, 2008, https://doi.org/10.1016/j.electacta.2008.04.023.

[2] T. G. Zavalis, M. Behm, and G. Lindbergh, "Investigations of Short-Circuit Scenarios in a Lithium-Ion Battery Cell," J. Electrochem. Soc., vol. 159, p. A848, 2012, http://dx.doi.org/10.1149/2.096206jes.

[3] Cai L, White R E. Mathematical modeling of a lithium ion battery with thermal effects in COMSOL Inc. Multiphysics (MP) software[J]. Journal of Power Sources, 2011, 196(14): 5985-5989, https://doi.org/10.1016/j.jpowsour.2011.03.017.

[4] Lu X, Bertei A, Finegan D P, et al. 3D microstructure design of lithium-ion battery electrodes assisted by X-ray nano-computed tomography and modelling[J]. Nature communications, 2020, 11(1): 1-13, https://doi.org/10.1038/s41467-020-15811-x.

[5] Zheng W, Shui M, Shu J I E, et al. GITT studies on oxide cathode $LiNi_{1/3}Co_{1/3}Mn_{1/3}O_2$ synthesized by citric acid assisted high-energy ball milling[J]. Bulletin of Materials Science, 2013, 36(3): 495-498, https://doi.org/10.1007/s12034-013-0480-1.

[6] Park M, Zhang X, Chung M, et al. A review of conduction phenomena in Li-ion batteries[J]. Journal of power sources, 2010, 195(24): 7904-7929, https://doi.org/10.1016/j.jpowsour.2010.06.060.

[7] Liu G, Zheng H, Kim S, et al. Effects of various conductive additive and polymeric binder contents on the performance of a lithium-ion composite cathode[J]. Journal of The Electrochemical Society, 2008, 155(12): A887, https://doi.org/10.1149/1.2976031.

[8] Danner T, Singh M, Hein S, et al. Thick electrodes for Li-ion batteries: A model based analysis[J]. Journal of Power Sources, 2016, 334: 191-201, https://doi.org/10.1016/j.jpowsour.2016.09.143.

[9] Ebner M, Geldmacher F, Marone F, et al. X-ray tomography of porous, transition metal oxide based lithium ion battery electrodes[J]. Advanced Energy Materials, 2013, 3(7): 845-850, https://doi.org/10.1002/aenm.201200932.